Running title: Loss of synchronized intra-islet Ca^{2+} oscillations *in vivo* in *Robo*-deficient β cells

Islet architecture controls synchronous β cell response to glucose in the intact mouse pancreas *in vivo*

Melissa T. Adams[1], Christopher A. Reissaus[2], Joseph M. Szulczewski[1], JaeAnn M. Dwulet[3], Melissa R. Lyman[1], Sophia M. Sdao[4], Sutichot D. Nimkulrat[1], Suzanne M. Ponik[1], Matthew J. Merrins[4], Richard K.P. Benninger[3], Raghavendra G. Mirmira[5], Amelia K. Linnemann[2], Barak Blum[1]*

[1]Department of Cell and Regenerative Biology, University of Wisconsin-Madison, Madison, WI 53705, USA

[2]Herman B Wells Center for Pediatric Research and Center for Diabetes and Metabolic Diseases, Indiana University School of Medicine, Indianapolis, IN 46202, USA

[3]Department of Bioengineering and Barbara Davis Center for Diabetes, University of Colorado Denver, Anschutz Medical Campus, Aurora, CO. 80045, USA

[4]Department of Medicine, Division of Endocrinology, Diabetes, and Metabolism, University of Wisconsin-Madison, Madison, Wisconsin 53705, USA

[5]Kovler Diabetes Center and the Department of Medicine, University of Chicago, Chicago, IL 60637, USA

***Lead contact and Corresponding Author:** Barak Blum; bblum4@wisc.edu

Abstract

The spatial architecture of the islets of Langerhans is hypothesized to facilitate synchronized insulin secretion between β cells, yet testing this *in vivo* in the intact pancreas is challenging. *Robo βKO* mice, in which the genes *Robo1* and *Robo2* are deleted selectively in β cells, provide a unique model of altered islet architecture without loss of β cell differentiation or islet damage from diabetes. Combining *Robo βKO* mice with intravital microscopy, we show here that *Robo βKO* islets lose synchronized intra-islet Ca^{2+} oscillations between β cells *in vivo*. We provide evidence that this loss is not due to a β cell-intrinsic function of Robo, loss of Connexin36 gap junctions, or changes in islet vascularization, suggesting that the islet architecture itself is required for synchronized Ca^{2+} oscillations. These results will have implications for understanding structure-function relationships in the islets during progression to diabetes as well as engineering islets from stem cells.

Introduction

The islets of Langerhans, which comprise the endocrine pancreas, are highly organized micro-organs responsible for maintaining blood glucose homeostasis. Islets are composed of five endocrine cell types (α, β, δ, PP, and ε) which, in rodents, are arranged such that the β cells reside in the core of the islet, while other non-β endocrine cells populate the islet mantle[1]. Human islet architecture is more complex; however, it still follows non-random patterning in which multiple core-mantle-like units comprise a single islet[2]. In both rodent and human islets, respective stereotypical islet architectures prioritize homotypic over heterotypic interactions between endocrine cell types[3]. The biological reason for preferential homotypic interactions between endocrine cells is not completely clear, but it has been suggested to be important for dictating the level of Connexin36 (Cx36)-mediated electrical β cell-β cell coupling, thus controlling synchronization of glucose-stimulated insulin secretion (GSIS) between neighboring β cells[4,5].

Synchronous insulin secretion between β cells is triggered when glucose from the blood enters the β cells through glucose transporters. As this glucose is metabolized, the ratio of intracellular ATP/ADP in the cells increases. The rise in ATP causes ATP sensitive K^+ channels to close, resulting in membrane depolarization. The resultant depolarization causes voltage-gated Ca^{2+} channels to open, triggering an influx of Ca^{2+} into the cell, which in turn promotes exocytosis of insulin granules[6-8]. This chain of events is cyclical and thus results in oscillations of membrane potential, cytosolic Ca^{2+} levels, and insulin secretion in response to glucose[9]. Because β cells within an islet are gap-junctionally coupled, and thus electrically coupled, these oscillations are synchronous across all islet β cells[10]. It is thus hypothesized that preferential β

cell homotypic contact allows for the necessary amount of gap junctions to form between neighboring β cells in order to synchronize the oscillations in an entire islet, facilitating pulsatile insulin secretion[5,11]. Indeed, modeling experiments in which the number of homotypic β cell-β cell nearest neighbor connections is lowered within an islet result in predicted perturbation of synchronous Ca^{2+} oscillations[5]. If this *in silico* prediction is correct, then disrupting spatial organization of the different endocrine cell types within the islet alone, without affecting any other property of the cells, should be sufficient to disturb synchronized insulin secretion between β cells. However, direct empirical evidence for this hypothesis is lacking.

Most genetic mouse models that show disruption of islet architecture also display defects in glucose homeostasis[12]. However, in many of these models, the disrupted islet architecture phenotype is linked to either developmental defects in β cell differentiation or maturation[13-24] or to pathologies related to β cell damage in diabetes[25-30]. This introduces a strong confounding factor for studying the role of islet architecture on β cell function. Therefore current mouse models of disrupted islet architecture unsuitable for directly testing the hypothesis that the preferential homotypic β cell-β cell interactions, dictated by canonical islet architecture, regulate synchronized insulin secretion between β cells within the same islet.

Recently, we have described a mouse model in which the cell-surface receptors *Robo1* and *Robo2* are deleted specifically in β cells (*Robo βKO*), resulting in disruption of canonical endocrine cell type sorting within the islets[31]. Unlike other models of disrupted islet architecture, the β cells in the islets of *Robo βKO* express normal levels of markers for β cell differentiation and functional maturity, and do not display markers of β cell damage or stress.

We reasoned that this model would allow us to directly test the role of islet architecture on synchronous islet oscillations between β cells in a fully differentiated, non-diabetic islet setting.

Results

Robo βKO islets express mature β cell markers despite having disrupted islet architecture and endocrine cell type intermixing

We have previously shown that genetic deletion of *Robo1* and *Robo2* selectively in β cells using either *Ins1-Cre; Robo1*$^{\Delta/\Delta}$*2*$^{flx/flx}$ or *Ucn3-Cre; Robo1*$^{\Delta/\Delta}$*2*$^{flx/flx}$ mice (*Robo βKO*) results in disrupted islet architecture and endocrine cell type sorting without affecting β cell death, proliferation, or the expression of the β cell maturation markers MafA and Ucn3[31]. To verify that β cells in *Robo βKO* islet are truly mature, we expanded the analysis to look at transcript levels of all maturity markers. We performed RNA sequencing and differential gene expression analysis on FACS-purified β cells from both *Robo βKO* and control islets, and observed no change in transcript levels of any hallmark β cell maturity or differentiation genes (*n*=2 mice of each genotype; **Supplemental Figure 1**). Thus, unlike other mouse models with disrupted islet architecture, β cells in *Robo βKO* islets maintain maturity and differentiation despite loss of normal islet architecture.

Robo βKO islets have fewer homotypic β cell-β cell contacts than control islets

In silico simulations where the degree of β cell-β cell coupling is changed through a decrease in homotypic nearest neighbors predict that disruption in islet architecture will disrupt synchronous intra-islet Ca^{2+} oscillations and hormone secretion pulses[3,5,32]. To test whether β

cells in *Robo βKO* islets have fewer homotypic β cell neighbors on average than control islets, we performed nearest neighbor analysis on islets from pancreatic sections from *Robo βKO* and control mice (**Figure 1**). We found that *Robo βKO* islets possess significantly fewer β cell-β cell contacts (*n*=9-11 islets for 3 mice from each genotype; control 75.35%, *Robo βKO* 50.37%, *p*=0.01), and homotypic contacts in general when compared to control islets (*n*=9-11 islets for 3 mice from each genotype; control 83.7%, *Robo βKO* 64.43%, *p*=0.0008). We also found that *Robo βKO* islets possess significantly more β cell-α cell contacts (*n*=9-11 islets for 3 mice from each genotype; control 11.21%, *Robo βKO* 25.99%, *p*=0.02), and heterotypic contacts in general when compared to control islets (*n*=9-11 islets for 3 mice from each genotype; control 16.3%, *Robo βKO* 35.57%, *p*=0.0008). Together, this suggests that *Robo βKO* islets make fewer homotypic β cell-β cell connections compared to control islets. We reasoned that the altered degree of homotypic β cell-β cell interaction in *Robo βKO* islets together with the seemingly retained β cell maturity provide a unique model by which to test the hypothesis that endocrine cell type organization affects synchronous insulin secretion in the islet.

Robo βKO* islets display unsynchronized Ca^{2+} oscillations *in vivo

To investigate how the reduced homotypic β cell-β cell connections in *Robo βKO* islets affects insulin-secretion dynamics, we adopted a novel intravital Ca^{2+} imaging method which enables imaging of islet Ca^{2+} dynamics *in situ* within the intact pancreas[33]. In brief, this method employs an intravital microscopy (IVM) platform and adeno-associated viral (AAV) delivery of insulin promoter-driven GCaMP6s, a fluorescent Ca^{2+} biosensor, to quantitate β cell Ca^{2+} dynamics *in vivo* in both *Robo βKO* and control islets. This method thus allows for retention of

the islet's *in vivo* microenvironment, blood flow, and innervation, and provides more realistic conditions than *in vitro* approaches allow for.

We verified that synchronous Ca^{2+} oscillations are maintained *in vivo* in islets by measuring GCaMP6s intensity of β cells within AAV8-RIP-GCaMP6 infected islets of control (*Robo WT*) mice (**Figure 2**). As expected, control mice displayed whole islet synchronous Ca^{2+} oscillations for at least 10 minutes after glucose elevation (*n*=3 islets from 1 mouse; **Figure 2** and **Supplemental Video 1**). We quantified the degree to which these oscillations are synchronous within the islet by analyzing the amount of correlation between GCaMP6s active areas within individual islets. While oscillations vary in frequency between islets, the degree of correlation between β cells within any one islet is very high, confirming that control islets possess highly synchronous intra-islet Ca^{2+} oscillation *in vivo* (fraction of GCAMP6s activity with correlated Ca^{2+} oscillations=0.97±0.005, n=3 islets from 1 mouse; see Figure 4A).

Conversely, we found that most *Robo βKO* islets display asynchronous intra-islet Ca^{2+} oscillations *in vivo* (**Figure 3, Supplemental Figure 2, Supplemental Videos 2 and 3**). Quantification of this asynchronous behavior through correlation analysis of GCaMP6s activity within individual *Robo βKO* islets revealed significant reduction in intra-islet correlated oscillation areas compared to controls (fraction of GCAMP6s activity with correlated Ca^{2+} oscillations=0.62±0.1, *n*=8 islets from 4 mice, $p<0.01$; **Figure 4A**). Further, asynchronous *Robo βKO* islets showed spatially distinct areas within the islet that oscillated synchronously with immediate β cell neighbors but not with more distant regions within the same islet (**Figure 3C-D, and Supplemental Figure 2**). This was not due to differences in the proportion of GCaMP6s positive cells showing elevated Ca^{2+} activity within *Robo βKO* islets compared to controls

(control islets 0.98±0.008 fraction active, *n*=3 islets from 1 mouse; *Robo βKO* islets 0.96±0.02 fraction active, *n*=5 islets from 3 mice, *p*=0.35; **Figure 4B**).

Interestingly, 3 out of the 8 *Robo βKO* islets imaged showed synchronous Ca^{2+} activity in greater than 90% of GCaMP6s positive areas (**Figure 4A, Supplemental Figure 3 and Supplemental video 4**). Moreover, upon performing organ clearing and imaging on *Robo βKO* pancreata, we observed multiple islets with relatively few α cells penetrating the β cell core (**Figure 5, Supplemental Videos 5 and 6**). It is likely that those *Robo βKO* islets with normal architecture are the same islets which retain synchronous Ca^{2+} oscillations. Together, these observations suggest that some mechanisms governing synchronous Ca^{2+} oscillations within an islet are not controlled intrinsically by Robo expression within β cells. This fits with the hypothesis that architecture of the islet itself facilitates synchronous oscillations.

Further, analysis of the speed of wave propagation and time lag in the highly correlated *Robo βKO* islets showed a trend towards a reduction in wave propagation speed (**Figure 4C**) and an increase in time lag (**Figure 4D**) when compared to controls, though these failed to reach the threshold for statistical significance (control islets wave propagation: 119.5±49.13μm/sec, *n*=3 islets from 1 mouse; *Robo βKO* islets wave propagation: 38.67±16.6μm/sec, *n*=3, *p*=0.1940; control islets phase lag: 0.057sec ±0.005, *n*=3 islets from 1 mouse: *Robo βKO* islets phase lag: 0.083±0.01sec, *n*=3, *p*=0.0934; **Figure 4C-F**). Islets with sub-optimal coupling have been shown to display full synchronization in Ca^{2+} oscillations, but with lower wave velocity[10]. Because there is a trend toward slower wave velocity, these *Robo βKO* islets may still have sub-optimal coupling due to architecture changes despite their fully synchronized Ca^{2+} oscillations.

Robo βKO islets retain the ability to form gap junctions and have similar levels of vascularization

Besides a decrease in β cell-β cell homotypic contacts within the islet, a possible explanation for the loss of synchronized whole islet Ca^{2+} oscillations in *Robo βKO* islets is that β cells in *Robo βKO* islets no longer possess the gap junctions necessary for adequate electrical coupling. Indeed, the phenotype described above is reminiscent of that observed in mice heterozygous for a *Cx36* null allele[10,34]. To test whether *Robo βKO* mice form fewer gap junctions between β cells, we measured the area of Cx36 protein immunofluorescence normalized to islet area in *Robo βKO* and control islets (**Figure 6**). We observed no difference in Cx36 immunofluorescence between *Robo βKO* islets and controls (**Figure 6B**), suggesting that loss of synchronous intra-islet Ca^{2+} oscillations is not due to failure of gap junction formation in β cells (control islets: 0.01±0.002 Cx36 signal/μm^2, *Robo βKO* islets: 0.01±0.001 Cx36 signal/μm^2, n=10-15, p=0.17 islets from 4 mice of each group).

Another possible explanation for the observed uncoupling of intra-islet Ca^{2+} oscillations in *Robo βKO* islets is that β cell-β cell contact in *Robo βKO* is disrupted due to physical blocking by non-endocrine tissue. To determine if other non-endocrine architectural changes within the islet occur in *Robo βKO* mice we quantified the amount of matrix components secreted by vessels as a surrogate for vasculature (laminin, and collagen IV) in *Robo βKO* and control islets. In all cases we found no significant difference in area of vessel matrix components (**Figure 7**) between *Robo βKO* and control islets, suggesting that interfering blood vessels are likely not the cause of loss of whole islet synchronous Ca^{2+} oscillations (normalized laminin β1 area: control 0.3126±0.05 μm^2, n=10-12 islets from 8 mice; *Robo βKO* 0.3747±0.05 μm^2, n=10-12 islets from 8

mice; p= 0.3908; normalized Col IV area: control 0.1812±0.01 μm^2, *n*=10-12 islets from 4 mice; *Robo βKO* 0.156±0.019, *p*=0.35).

Discussion

In this study, we provide evidence for the importance of islet architecture for proper islet function *in vivo*. When islet architecture is disrupted while β cell maturity is retained in *Robo βKO* mice, synchronized Ca^{2+} oscillations are perturbed in the *in vivo* islet. This is not due to loss of Cx36, or change in amount of islet vascularization. *Robo βKO* β cells possess fewer homotypic nearest neighbors than controls, suggesting a limited capacity to electrically couple β cells across the islet. Taken together, these data indicate that islet architecture itself, uncoupled from β cell maturity or availability of gap junction machinery is important for coordinated insulin secretion between β cells.

Robo, and its ligand Slit, have been previously shown to affect Ca^{2+} oscillations in β cell *in vitro*[35]. However, while it is possible that intrinsic β cell factors rather than the disrupted islet architecture alone contribute to disruption of synchronized Ca^{2+} oscillations in *Robo βKO* islets in our experiments, this is not likely the driving force. If this was the case, then we would expect a highly penetrant asynchronous oscillation phenotype in *Robo βKO* islets, yet more than one-third of *Robo βKO* islets analyzed showed highly synchronized Ca^{2+} oscillations. Instead, these results suggest that deletion of *Robo* alone in β cells is not sufficient to abolish synchronicity. Moreover, *Robo βKO* islets show a heterogeneous spectrum of disrupted architecture within the same animal, with some islets displaying severe endocrine cell type intermixing while others retain relatively normal architecture. Thus it is likely that islets with relatively normal

architecture correspond to the islets that display more synchronous Ca^{2+} oscillations. Moreover phenotypic heterogeneity is likely not due to an incomplete deletion of *Robo* in a subset of islets. This is evident by the fact the islets were detected during the Ca^{2+} imaging experiment by the fluorescent labeling of β cells with the H2B-mCherry lineage-tracing reporter[31], which uses the same Cre that is used to delete *Robo* in those β cells. Thus expression of H2B-mCherry precludes inefficient Cre expression and recombination.

It also remains possible that other components of islet architecture besides endocrine cell type sorting contribute to disruption in Ca^{2+} oscillations found in *Robo βKO* islets. Specifically, while we have shown that the amount of vascularization between *Robo βKO* islets and controls is similar, we cannot draw conclusions on whether the pattern of vessels is unchanged. Further, it is possible that amount and patterning of innervation may vary between *Robo βKO* and controls. This is particularly of interest because *Robo* has known roles in angiogenesis and axon guidance, and thus could affect precisely how the islet is innervated and vascularized[36].

Finally, our results may have implications towards directing islet architecture in the pursuit of generating *bona fide* islets from stem cells *in vitro* for the treatment of diabetics. Thus far, most efforts to create such stem cell derived islets have focused on creating homogenous functionally mature β cells[37]. Such efforts have been largely successful in terms of creating β cells that display insulin secretory profiles close to those of primary β cells[38]. Yet despite their seeming resemblance to mature native β cells, islets made from stem cell-derived β cells fail to fully match the function of isolated primary islets[37,38]. This has been partially attributed to the fact that stem cell derived islets formed *in vitro* thus far have been simply

clusters of homogenous β cells, rather than an organized heterogeneous population of β cells and other islet cell types[37]. Because of the importance of heterogeneous cell types in controlling glucose homeostasis, it has become evident that achieving correct β cell heterogeneity is needed to generate better islets *in vitro*[39]. However, it is likely that addition of these cells without recapitulation of islet architecture will not generate islets with optimum function and β cell coupling.

Acknowledgments

We Kurt Weiss and Jan Huisken for help with imaging. We thank members of the Blum lab, especially Jennifer Gilbert and Bayley Waters, for valuable discussion. We are also grateful to Nadav Sharon and Danny Ben-Zvi for critically reading the manuscript. This work was funded in part by the following grants. R01DK121706, the DRC at Washington University Pilot Grant P30DK020579, and Pilot Award UL1TR000427 from the UW-Madison Institute for Clinical and Translational Research (ICTR) to BB; R01DK060581 to RM; R01DK102950 and R01DK106412 to RKPB; R01CA216248 to SP; R01DK113103, R01AG062328, ADA 1-16-IBS-212 to MM, and an award from the Wisconsin Partnership Program to BB and MM. MTA was funded by 5T32GM007133-44 and a graduate training award from the UW-Madison Stem Cell & Regenerative Medicine Center. We also thank the University of Wisconsin Carbone Cancer Center Support Grant P30CA014520 for use of the UW Flow Core, and the University of Wisconsin, Madison Biotechnology Center for sequencing and analysis.

Author Contribution

Conceptualization, B.B. and M.T.A; Methodology, B.B., M.T.A., C.A.R, and J.M.D.; Investigation, M.T.A., C.A.R, J.M.S, M.R.L, S.M.S, and S.D.N; Formal Analysis, M.T.A., C.A.R, M.R.L., and J.M.D.; Resources, S.M.P, R.G.M, A.K.L, M.J.M. and R.K.P.B.; Writing Original Draft, B.B and M.T.A.; Writing, Review and Editing, all authors; Funding Acquisition, B.B., S.M.P, M.J.M, R.K.P.B., R.G.M., and A.K.L; Supervision, B.B.

Materials and Methods

Animals

The experimental protocol for animal usage was reviewed and approved by the University of Wisconsin-Madison Institutional Animal Care and Use Committee (IACUC) under Protocol #M005221 and Protocol #M005333, and all animal experiments were conducted in accordance with the University of Wisconsin-Madison IACUC guidelines under the approved protocol. *Robo1*$^{\Delta}$,*2*^{flx40}, *Ins1-Cre*[41], *Urocortin3-Cre*[42] and *Rosa26-Lox-Stop-Lox-H2BmCherry*[43] mice were previously described. All mouse strains were maintained on a mixed genetic background. Control colony mates in all analyses were *Robo*$^{+/+}$ with the either *Ins1-Cre or Ucn3-Cre*.

Immunofluorescence

Pancreata were fixed with 4% PFA at 4°C for 3h, embedded in 30% sucrose and frozen in OCT (Tissue-Tek). Pancreatic sections (10 µm) were stained using a standard protocol. The following primary antibodies and dilutions were used: guinea pig anti-Insulin (1:6, Dako, IR00261-2), mouse anti-Glucagon (1:500, Sigma G2654), rabbit anti-Glucagon (1:200, Cell Signaling 2760S), rabbit anti-Somatostatin (1:1000, Phoenix G-060-03), rabbit anti-Connexin36 (1:80, Invitrogen 36-4600), rabbit anti-Col IV (1:300, Abcam Ab656), rat anti-Laminin β1 (1:500, Invitrogen MA5-14657). The following secondary antibodies were used at 1:500: Donkey anti-Guinea Pig 594 (Jackson), Donkey anti-Guinea Pig 647 (Jackson), Donkey anti-Rabbit 488 (Invitrogen), Donkey anti-Rabbit 594 (Invitrogen), Donkey anti-goat 647 (Invitrogen), and Donkey anti-rat 488

(Invitrogen). Slides were imaged using a Leica SP8 Scanning Confocal microscope or a Zeiss Axio Observer.Z1 microscope.

RNA sequencing

RNA was isolated from FACS sorted lineage-traced β cells[31] from control and *Robo βKO* mice using phenol chloroform extraction (TRIzol). DNA libraries were generated using Takara's SMART-Seq v4 Low Input RNA Kit for Sequencing (Takara, Mountain View, California, USA) for cDNA synthesis and the Illumina NexteraXT DNA Library Preparation (Illumina, San Diego, CA, USA) kit for cDNA dual indexing. Full length cDNA fragments were generated from 1-10ng total RNA by SMART (Switching Mechanism at 5' End of RNA Template) technology. cDNA fragments were fragmented and dual indexed in a single step using the Nextera kit's simultaneous transposon and tagmentation step. Quality and quantity of completed libraries were assessed using Agilent DNA series chip assay (Agilent Technologies, Santa Clara, CA) and Invitrogen Qubit ds DNA HS Kit (Invitrogen, Carlsbad, California, USA), respectively. Each library was standardized to 2nM. Cluster generation was performed on Illumina cBot, with libraries multiplexed for 1x100bp sequencing using TruSeq 100bp SBS kit (v4) on an Illumina HiSeq2500. Images were analyzed using standard Illumina Pipeline, version 1.8.2.

Intravital Imaging

Mouse pancreata were exposed in anesthetized mice by making a small incision on the right side of the mouse, and externalizing the tip of the pancreas. A glass dish was placed over the exposed pancreas and the mouse was placed on a microscope stage with isoflurane anesthesia

for the remainder of imaging. Islets were identified on the surface of the pancreas by detecting Histone H2BmCherry fluorescent nuclei labeled by β cell-specific lineage-tracing reporter[31]. Once islets were identified, mice were given injections of 1g/kg body weight glucose (30% in saline) intraperitoneally. Blood glucose levels were monitored through tail vein bleeds. Once the blood glucose reached ~300 mg/dL, GCaMP6s activity was identified using the microscope eye piece. When imaging a time course of GCaMP6s intensity, a z-stack was set to 8 or 12 slices each 8µm apart. Images were captured every 10 or 30 seconds respectively over 10 minutes at a resolution of 512x512 pixels. After time courses were recorded, high resolution image z-stacks were taken with 60 z planes taken 1µm apart or 8 z-planes taken 8µm apart at 1024x1024 pixel resolution. For some images, rhodamine-dextran was injected retro-orbitally to mark the vasculature of the islets *in vivo.*

Gap junction and vasculature quantification

Cx36 levels were quantified from images of islets co-stained with rabbit anti-Cx36 (Invitrogen) and Guinea Pig anti-insulin antibody. Vasculature levels were quantified from images co-stained with rat anti-Laminin β1 or rabbit anti-col IV and guinea pig anti-insulin. 8 Z-planes were taken 1µm apart on a Leica SP8 Scanning Confocal microscope using a 40x oil immersion objective (Cx36) or 20X (vasculature). Threshold masks were made of both channels for each islets, and the area of each staining was measured using FIJI's analyze particles functions. The area of gap junctions, blood vessels (marked by their respective antibody) was divided by the area of insulin for each islet. 10-14 islets were analyzed for n=2-8 mice for each genotype. Student's T-test was performed to obtain P values.

Nearest Neighbor Analysis

β cells were identified using the lineage tracer *Rosa26-Lox-Stop-Lox-H2BmCherry* crossed to *Ucn3-Cre* and tissue sections were stained with antibodies against glucagon and somatostatin to identify α and δ cells respectively. The 3D Tissue Spatial Analysis Toolbox for Fiji[44] was used to identify specific cell types using the above markers and to calculate the number of cell type specific nearest neighbors from all identified endocrine cells. Analysis was performed on 9-11 islets from *n*=3 mice from each genotype.

Whole Organ Clearing and Imaging

Pancreata were fixed in 4% PFA for 3 hours at room temperature, then dehydrated stepwise in methanol (33, 66%, and 100%) for 15 mins each step. Samples were then bleached using MeOH:H_2O_2:DMSO bleaching buffer in a 2:1:3 ratio at RT for 24 hr, and then stored in methanol overnight. Next, Samples were freeze-thawed for at least 5 cycles of 24 hour freeze then 2 hour thaw in -80°C-RT to facilitate antibody penetration. Samples were then rehydrated stepwise back to TBST (33%, 66%, 100%), at least 15 min/step, reducing the MeOH during each step. Samples were then blocked in TBST with 10% donkey serum, 5% DMSO and 0.01% NaAz for 12-24 hr at RT. Samples were then incubated with primary antibodies (Dako guinea pig anti-Insulin and CST Rabbit anti-glucagon) in blocking buffer for 48 hr- 72 hr, then washed overnight in TBST. Following wash, samples were incubated with secondary antibodies (594 anti-glucagon and 647 anti-insulin) for 48-72 hr at RT, then washed overnight in TBST. Whole pancreata were then mounted in low melting temp agarose for imaging. Whole pancreata were imaged using a

custom light sheet microscope. 2D images were collected in a 3 mm x 5 mm field of view every 10 um over a 5 mm volume to generate the 3D reconstruction. Imaris was used to assign surface volumes to pancreas morphology, insulin surfaces, and glucagon surfaces by intensity thresholding.

Time Course Image Analysis

All images were analyzed using previously published methods[45] with custom Matlab (Mathworks) scripts. For activity analysis, images were smoothed using a 5x5 pixel averaging filter. Areas without significant fluorescence were removed. Saturated areas were also removed by limiting the area to intensity below the maximum value. Photobleaching was adjusted for by removing any linear trend. Any islets with significant motion artifacts were removed or time courses were shortened to the time over which no significant movement occurred (displacement of <0.5 cell width). For the time course of each pixel in the image with significant fluorescence, a peak detection algorithm was used to determine if the areas had peak amplitudes significantly above background. A region was considered “active” if the corresponding time course for each pixel had a peak amplitude >2.4x background. The fraction of active area was calculated as the number of pixels detected as “active” across all z-planes, normalized to the total number of pixels that showed significant fluorescence across all z-planes that were not saturated. Islets with significant background fluorescence from spectral overlap of channels were excluded from activity analysis because “inactive” cells were indistinguishable from background and therefore total islet area could not be accurately calculated. Coordination was determined based on coincident timing of identified peaks, where

areas were segmented by identified peaks occurring at similar time points. The cross correlation of the time courses for two 5x5 pixel subregion was taken. If the correlation coefficient was >0.75, then the two subregions were considered highly coordinated and merged into a larger region. The coordinated area was calculated as the number of pixels in the largest area of coordination across all z-planes normalized to the total number of pixels of the islet that were determined to be 'active' for all planes. This analysis is based on previous analysis[45], but adjusted for 3-dimensional data. Phase lag and wave propagation speed was determined as in[10], where 2 regions were chosen manually within a coordinated area within the same z-plane. The phase lag of these regions was calculated from a Fourier transform of each time course. First the peak frequency was identified from the power spectrum, as generated from a Fourier transform of each time course. At each peak frequency the phase was then calculated. The phase lag was calculated from the difference in phase between each region, and converted into a time lag according to $(dt{=}(1f){*}tan{-}1(\varphi 1{-}\varphi 2))$, where $\varphi 1{-}\varphi 2$ is the phase difference, and f is the sampling frequency of the time courses analyzed. Speed was calculated by dividing the distance between the two regions by the time lag. For phase and speed analysis only islets with >90% coordinated area was used. All statistical analysis was performed in Prism (Graphpad) or Matlab. First a F-test was used to determine if variances were equal then a Student's t-test or Welch t-test (for unequal variance) were utilized for determining whether activity, coordination, phase lag and speed were significantly different. $p<0.05$ was considered significant.

Figure Legends

Figure 1: *Robo βKO* islets have fewer homotypic nearest neighbors than controls (A) Immunofluorescence images (left and middle panels) and cell connectivity maps generated by nearest neighbor analysis (right panels) of control and *Robo βKO* islets. β cells (red), α cells (green), and δ cells (blue) are denoted by nodes on the connectivity maps. A line the same color as both nodes it connects denotes a homotypic interaction of that corresponding cell type. A white line connecting two nodes denotes a heterotypic interaction between cell types. (B) Probability of any homotypic cell-cell contact in *Robo βKO* islets vs controls (*n*=9-11 islets for 3 mice from each genotype; control 83.7%, *Robo βKO* 64.43%, *p* 0.0008). (C) Probability of β cell-β cell contacts in *Robo βKO* islets *vs*. controls (*n*=9-11 islets for 3 mice from each genotype; control 75.35%, *Robo βKO* 50.37%, *p*=0.01). (D) Probability of any heterotypic cell-cell contact in *Robo βKO* islets *vs*. controls (*n*= 9-11 islets for 3 mice from each genotype; control 16.3%, *Robo βKO* 35.57%, *p*=0.0008 (E). Probability of β cell- α cell contacts in *Robo βKO* islets vs controls (*n*=9-11 islets for 3 mice from each genotype; control 11.21%, *Robo βKO* 25.99%, *p*=0.02). (B-E Similar shaded points in graphs indicate islets from the same mouse).

Figure 2: Control islets show highly synchronized whole islet Ca^{2+} oscillations (A) High resolution maximum intensity projection of a control islet *in vivo* in an *AAV8-RIP-GCaMP6s*-injected mouse showing GCaMP6s in green, nuclear mCherry β cell lineage-tracing in red, and collagen (second-harmonic fluorescence) in blue. (B) Stills over one oscillation period from control islet in supplementary video 1, starting after blood glucose level reached ~300 mg/dL from IP glucose injection. Video was recorded for 10 minutes with frames taken every 10

seconds. (C) Representative time courses of Ca^{2+} activity in 4 individual areas from control islet in supplementary video 1 showing correlation over 98% of the active islet area. Time courses are normalized to average fluorescence of individual area over time. Similar color indicates that the time courses have a Pearson's correlation coefficient of ≥0.75 and matches the region of coordination that is seen in D. (D) False color map of top five largest coordinated areas across z-stack of control islet from analysis in C. Areas in grey are not coordinated. The color represents a region of coordination with Pearson's Correlation Coefficient ≥0.75 of GCaMP6s activity. Cells used in time courses in C are labeled.

Figure 3: *Robo βKO* islets show uncoordinated whole islet Ca^{2+} oscillations (A) High resolution maximum intensity projection of a *Robo βKO* islet *in vivo* in an *AAV8-RIP-GCaMP6s*-injected mouse showing GCaMP6s in green, nuclear mCherry β cell lineage tracing in red, and collagen in blue. (B) Stills over one oscillation period from *Robo βKO* islet in supplementary video 2, starting after blood glucose level reached ~300 mg/dL from IP glucose injection. Video was recorded for 10 minutes with frames taken every 30 seconds. (C) Representative time courses of Ca^{2+} activity in 4 individual areas from *Robo βKO* islet in supplementary video 2, showing correlation of 43.6% of the active islet area. Time courses are normalized to average fluorescence of individual area over time. Similar color indicates that the time courses have a Pearson's correlation coefficient of ≥0.75 and matches the region of coordination that is seen in D. (D) False color map of top five largest coordinated areas across z-stack of *Robo βKO* islet from analysis in C. Areas in grey are not coordinated. The color represents a region of

coordination with Pearson's Correlation Coefficient ≥0.75 of GCaMP6s activity. Cells used in time courses in C are labeled.

Figure 4: Quantification of *Robo βKO* Ca^{2+} oscillation phenotype *(*A) Largest fraction of area in islet exhibiting coordinated Ca^{2+} oscillations for control and *Robo βKO* islets. (B) Fraction of active islet area showing elevated Ca^{2+} activity for control and *Robo βKO* islets. (C) Phase lag of islet from control and *Robo βKO* islets. Only islets with large coordination across islet (>90% coordinated area) were used. (D) Speed across islets from control and *Robo βKO* islets. Only islets with large coordination across islet (>90% coordinated area) were used. (E) Close up of time-courses from islet in Figure 2, showing representative phase lag of Ca^{2+} waves of 2 cells in the same z-plane. (F) Same as C but for Supplemental Figure 3.

Figure 5*: Robo βKO* islets show heterogeneity in severity of architectural disruption (A) Space filling models generated from cleared 3x5mm sections of pancreatic tissue from control and *Robo βKO* mice with insulin in red, glucagon in green, and auto-fluorescent surrounding tissue in blue. Projections show surface views of islets with insulin channel shown as transparent in order to visualize α cells on the adjacent side and the interior of the islet. (B) Close ups from portions of the pancreatic tissue showing heterogeneity in architectural phenotype in *Robo βKO* and number of α cells present in both control and *Robo βKO.*

Figure 6: Amount of Cx36 gap junctions remains unchanged in *Robo βKO* (A) Immunofluorescent images showing Cx36 (gray or green) and insulin (red) in *Robo βKO* and

452 control islets. (B) Quantification of area of Cx36 staining normalized to islet area in *Robo βKO*
453 islets and controls showing no significant difference (*n*=10-12 islets for 4 mice per group,
454 *p*=0.17).
455
456 **Figure 7: Amount of vascularization remains unchanged in *Robo βKO* islets** (A) Representative
457 immunofluorescent staining of basement membrane marking vasculature (laminin and collagen
458 IV) showing similar amounts in *Robo βKO* and control islets (B) Quantification of area of staining
459 normalized to islet area showing no difference in amounts of basement membrane marking
460 blood vessels in *Robo βKO* compared to control islets.

Supplemental Figures

Supplemental Video 1: Control islets show highly synchronized Ca^{2+} oscillations. Intravital time course video of an islet within the *in vivo* pancreas of a control β cell lineage traced mouse infected with *AAV8-Ins1-GCaMP6s*. Lineage traced β cells are marked by mCherry in red and GCaMP6s is shown in green. Mouse was injected IP with glucose, and video was recorded once blood glucose levels reached ~300 mg/dL. Images were taken every 10 seconds through a Z-stack of 8 slices each 8µm apart, over 10 minutes. Scale bar is 100µm. Time stamp shown in in upper left corner shows time of image in min:sec.

Supplemental Video 2: *Robo βKO* islets show unsynchronized Ca^{2+} oscillations. Intravital time course video of an islet within the *in vivo* pancreas of a *Robo βKO* β cell lineage traced mouse infected with *AAV8-Ins1-GCaMP6s*, and retro-orbitally injected with rhodamine-dextran to mark vasculature. Lineage traced β cells are marked by mCherry in red and GCaMP6s is shown in green, and vasculature is shown in yellow. Mouse was injected IP with glucose, and video was recorded once blood glucose levels reached ~300 mg/dL. Images were taken every 30 seconds through a Z-stack of 12 slices each 8µm apart, over 10 minutes. Scale bar is 100µm. Time stamp shown in in upper left corner shows time of image in min:sec.

Supplemental Video 3: Most *Robo βKO* islets show unsynchronized Ca^{2+} oscillations. Intravital time course video of an islet within the *in vivo* pancreas of a *Robo βKO* β cell lineage traced mouse infected with *AAV8-Ins1-GCaMP6s*. Lineage traced β cells are marked by mCherry in red and GCaMP6s is shown in green. Mouse was injected IP with glucose, and video was recorded

once blood glucose levels reached ~300 mg/dL. Images were taken every 10 seconds through a Z-stack of 8 slices each 8µm apart, over 10 minutes. Scale bar is 100µm. Time stamp shown in in upper left corner shows time of image in min:sec.

Supplemental Video 4: A subset of *Robo βKO* islets retain synchronized Ca^{2+} oscillations. Intravital time course video of an islet within the *in vivo* pancreas of a *Robo βKO* β cell lineage traced mouse infected with AAV8-Ins1-GCaMP6s. Lineage traced β cells are marked by mCherry in red and GCaMP6s is shown in green. Mouse was injected IP with glucose, and video was recorded once blood glucose levels reached ~300 mg/dL. Images were taken every 10 seconds through a Z-stack of 8 slices each 8µm apart, over 10 minutes. Scale bar is 100µm. Time stamp shown in in upper left corner shows time of image in min:sec.

Supplemental Figure 1: *Robo βKO* islets retain β cell differentiation and maturity markers Volcano plot of differential gene expression from bulk RNA sequencing on lineage traced FACS sorted β cells from *Robo βKO* and control mice showing no significant differential gene expression of markers (*n*=2 mice from each group).

Supplemental Figure 2: *Robo βKO* islets show uncoordinated whole islet Ca^{2+} oscillations (A) High resolution maximum intensity projection of a *Robo βKO* islet *in vivo* in an *AAV8-RIP-GCaMP6s*-injected mouse showing GCaMP6s in green, nuclear mCherry β cell lineage-tracing in red, and collagen (second-harmonic fluorescence) in blue. (B) Stills over one oscillation period from *Robo βKO* islet in supplemental video 2, starting after blood glucose level reached ~300

mg/dL from IP glucose injection. Video was recorded for 10 minutes with frames taken every 10 seconds. (C) Representative time courses of Ca^{2+} activity in 4 individual areas from *Robo βKO* islet in supplementary video 3, showing correlation of 50% of the active islet area. Time courses are normalized to average fluorescence of individual area over time. Similar color indicates that the time courses Similar color indicates that the time courses have a Pearson's correlation coefficient of ≥0.75 and matches the region of coordination that is seen in D. (D) False color map of top five largest coordinated areas across z-stack of *Robo βKO* islet from analysis in C. Areas in grey are not coordinated. The color represents a region of coordination with Pearson's correlation coefficient of ≥0.75 of GCaMP6s activity.

Supplemental Figure 3: A subset of *Robo βKO* islets show coordinated whole islet Ca^{2+} oscillations (A) High resolution maximum intensity projection of a *Robo βKO* islet *in vivo* in an *AAV8-RIP-GCaMP6s*-injected mouse showing GCaMP6s in green, nuclear mCherry β cell lineage tracing in red, and collagen in blue. (B) Stills over one oscillation period from *Robo βKO* islet in supplementary video 4, starting after blood glucose level reached ~300 mg/dL from IP glucose injection. Video was recorded for 10 minutes with frames taken every 10 seconds. (C) Representative time courses of Ca^{2+} activity in 4 individual areas from *Robo βKO* islet in supplementary video 4, showing correlation of 98% of the active islet area. Time courses are normalized to average fluorescence of individual area over time. Similar color indicates that the time courses have a Pearson's correlation coefficient of ≥0.75 and matches the region of coordination that is seen in D. (D) False color map of top five largest coordinated areas across z-stack of *Robo βKO* islet from analysis in C. Areas in grey are not coordinated. The color

represents a region of coordination with Pearson's correlation coefficient of ≥0.75 of GCaMP6s activity.

References

1 Kim, A. *et al.* Islet architecture: A comparative study. *Islets* **1**, 129-136, doi:10.4161/isl.1.2.9480 (2009).

2 Bonner-Weir, S., Sullivan, B. A. & Weir, G. C. Human Islet Morphology Revisited: Human and Rodent Islets Are Not So Different After All. *The journal of histochemistry and cytochemistry : official journal of the Histochemistry Society* **63**, 604-612, doi:10.1369/0022155415570969 (2015).

3 Hoang, D. T. *et al.* A conserved rule for pancreatic islet organization. *PloS one* **9**, e110384, doi:10.1371/journal.pone.0110384 (2014).

4 Hraha, T. H., Bernard, A. B., Nguyen, L. M., Anseth, K. S. & Benninger, R. K. Dimensionality and size scaling of coordinated Ca(2+) dynamics in MIN6 beta-cell clusters. *Biophysical journal* **106**, 299-309, doi:10.1016/j.bpj.2013.11.026 (2014).

5 Nittala, A., Ghosh, S. & Wang, X. Investigating the role of islet cytoarchitecture in its oscillation using a new beta-cell cluster model. *PloS one* **2**, e983, doi:10.1371/journal.pone.0000983 (2007).

6 Ammala, C. *et al.* Exocytosis elicited by action potentials and voltage-clamp calcium currents in individual mouse pancreatic B-cells. *The Journal of physiology* **472**, 665-688, doi:10.1113/jphysiol.1993.sp019966 (1993).

7 Ashcroft, F. M. & Rorsman, P. K(ATP) channels and islet hormone secretion: new insights and controversies. *Nature reviews. Endocrinology* **9**, 660-669, doi:10.1038/nrendo.2013.166 (2013).

8 Bertram, R., Sherman, A. & Satin, L. S. Electrical bursting, calcium oscillations, and synchronization of pancreatic islets. *Advances in experimental medicine and biology* **654**, 261-279, doi:10.1007/978-90-481-3271-3_12 (2010).

9 Bertram, R., Satin, L. S. & Sherman, A. S. Closing in on the Mechanisms of Pulsatile Insulin Secretion. *Diabetes* **67**, 351-359, doi:10.2337/dbi17-0004 (2018).

10 Benninger, R. K., Zhang, M., Head, W. S., Satin, L. S. & Piston, D. W. Gap junction coupling and calcium waves in the pancreatic islet. *Biophysical journal* **95**, 5048-5061, doi:10.1529/biophysj.108.140863 (2008).

11 Head, W. S. *et al.* Connexin-36 gap junctions regulate in vivo first- and second-phase insulin secretion dynamics and glucose tolerance in the conscious mouse. *Diabetes* **61**, 1700-1707, doi:10.2337/db11-1312 (2012).

12 Brereton, M. F., Vergari, E., Zhang, Q. & Clark, A. Alpha-, Delta- and PP-cells: Are They the Architectural Cornerstones of Islet Structure and Co-ordination? *The journal of histochemistry and cytochemistry : official journal of the Histochemistry Society* **63**, 575-591, doi:10.1369/0022155415583535 (2015).

13 Hang, Y. *et al.* The MafA transcription factor becomes essential to islet beta-cells soon after birth. *Diabetes* **63**, 1994-2005, doi:10.2337/db13-1001 (2014).

14 Yamagata, K. *et al.* Overexpression of dominant-negative mutant hepatocyte nuclear fctor-1 alpha in pancreatic beta-cells causes abnormal islet architecture with decreased expression of E-cadherin, reduced beta-cell proliferation, and diabetes. *Diabetes* **51**, 114-123 (2002).

15 Gannon, M. *et al.* Persistent expression of HNF6 in islet endocrine cells causes disrupted islet architecture and loss of beta cell function. *Development* **127**, 2883-2895 (2000).

16 Gu, C. *et al.* Pancreatic beta cells require NeuroD to achieve and maintain functional maturity. *Cell metabolism* **11**, 298-310, doi:10.1016/j.cmet.2010.03.006 (2010).

17 Ahlgren, U., Jonsson, J., Jonsson, L., Simu, K. & Edlund, H. beta-cell-specific inactivation of the mouse Ipf1/Pdx1 gene results in loss of the beta-cell phenotype and maturity onset diabetes. *Genes & development* **12**, 1763-1768 (1998).

18 Borden, P., Houtz, J., Leach, S. D. & Kuruvilla, R. Sympathetic innervation during development is necessary for pancreatic islet architecture and functional maturation. *Cell reports* **4**, 287-301, doi:10.1016/j.celrep.2013.06.019 (2013).

19 Doyle, M. J. & Sussel, L. Nkx2.2 regulates beta-cell function in the mature islet. *Diabetes* **56**, 1999-2007, doi:10.2337/db06-1766 (2007).

20 Sinagoga, K. L. *et al.* Distinct roles for the mTOR pathway in postnatal morphogenesis, maturation and function of pancreatic islets. *Development* **144**, 2402-2414, doi:10.1242/dev.146316 (2017).

21 Huang, C. *et al.* Synaptotagmin 4 Regulates Pancreatic beta Cell Maturation by Modulating the Ca(2+) Sensitivity of Insulin Secretion Vesicles. *Developmental cell* **45**, 347-361 e345, doi:10.1016/j.devcel.2018.03.013 (2018).

22 Jimenez-Caliani, A. J. *et al.* alphaE-Catenin Is a Positive Regulator of Pancreatic Islet Cell Lineage Differentiation. *Cell reports* **20**, 1295-1306, doi:10.1016/j.celrep.2017.07.035 (2017).

23 Bastidas-Ponce, A. *et al.* Foxa2 and Pdx1 cooperatively regulate postnatal maturation of pancreatic beta-cells. *Molecular metabolism* **6**, 524-534, doi:10.1016/j.molmet.2017.03.007 (2017).

24 Crawford, L. A. *et al.* Connective tissue growth factor (CTGF) inactivation leads to defects in islet cell lineage allocation and beta-cell proliferation during embryogenesis. *Mol Endocrinol* **23**, 324-336, doi:10.1210/me.2008-0045 (2009).

25 Szabat, M. *et al.* Reduced Insulin Production Relieves Endoplasmic Reticulum Stress and Induces beta Cell Proliferation. *Cell metabolism* **23**, 179-193, doi:10.1016/j.cmet.2015.10.016 (2016).

26 Brissova, M. *et al.* Islet microenvironment, modulated by vascular endothelial growth factor-A signaling, promotes beta cell regeneration. *Cell metabolism* **19**, 498-511, doi:10.1016/j.cmet.2014.02.001 (2014).

27 Baetens, D. *et al.* Alteration of islet cell populations in spontaneously diabetic mice. *Diabetes* **27**, 1-7 (1978).

28 Starich, G. H., Zafirova, M., Jablenska, R., Petkov, P. & Lardinois, C. K. A morphological and immunohistochemical investigation of endocrine pancreata from obese ob+/ob+ mice. *Acta histochemica* **90**, 93-101, doi:10.1016/S0065-1281(11)80167-4 (1991).

29 Kilimnik, G. *et al.* Altered islet composition and disproportionate loss of large islets in patients with type 2 diabetes. *PloS one* **6**, e27445, doi:10.1371/journal.pone.0027445 (2011).

30 Nir, T., Melton, D. A. & Dor, Y. Recovery from diabetes in mice by beta cell regeneration. *The Journal of clinical investigation* **117**, 2553-2561, doi:10.1172/JCI32959 (2007).

31 Adams, M. T., Gilbert, J. M., Hinojosa Paiz, J., Bowman, F. M. & Blum, B. Endocrine cell type sorting and mature architecture in the islets of Langerhans require expression of Roundabout receptors in beta cells. *Scientific reports* **8**, 10876, doi:10.1038/s41598-018-29118-x (2018).

32 Hoang, D. T., Hara, M. & Jo, J. Design Principles of Pancreatic Islets: Glucose-Dependent Coordination of Hormone Pulses. *PloS one* **11**, e0152446, doi:10.1371/journal.pone.0152446 (2016).

33 Reissaus, C. A. *et al.* A Versatile, Portable Intravital Microscopy Platform for Studying Beta-cell Biology In Vivo. *Scientific reports* **9**, 8449, doi:10.1038/s41598-019-44777-0 (2019).

34 Ravier, M. A. *et al.* Loss of connexin36 channels alters beta-cell coupling, islet synchronization of glucose-induced Ca2+ and insulin oscillations, and basal insulin release. *Diabetes* **54**, 1798-1807 (2005).

35 Yang, Y. H., Manning Fox, J. E., Zhang, K. L., MacDonald, P. E. & Johnson, J. D. Intraislet SLIT-ROBO signaling is required for beta-cell survival and potentiates insulin secretion. *Proceedings of the National Academy of Sciences of the United States of America* **110**, 16480-16485, doi:10.1073/pnas.1214312110 (2013).

36 Blockus, H. & Chedotal, A. Slit-Robo signaling. *Development* **143**, 3037-3044, doi:10.1242/dev.132829 (2016).

37 Sneddon, J. B. *et al.* Stem Cell Therapies for Treating Diabetes: Progress and Remaining Challenges. *Cell stem cell* **22**, 810-823, doi:10.1016/j.stem.2018.05.016 (2018).

38 Nasteska, D., Viloria, K., Everett, L. & Hodson, D. J. Informing beta-cell regeneration strategies using studies of heterogeneity. *Molecular metabolism* **27S**, S49-S59, doi:10.1016/j.molmet.2019.06.004 (2019).

39 Roscioni, S. S., Migliorini, A., Gegg, M. & Lickert, H. Impact of islet architecture on beta-cell heterogeneity, plasticity and function. *Nature reviews. Endocrinology* **12**, 695-709, doi:10.1038/nrendo.2016.147 (2016).

40 Branchfield, K. *et al.* Pulmonary neuroendocrine cells function as airway sensors to control lung immune response. *Science* **351**, 707-710, doi:10.1126/science.aad7969 (2016).

41 Thorens, B. *et al.* Ins1(Cre) knock-in mice for beta cell-specific gene recombination. *Diabetologia* **58**, 558-565, doi:10.1007/s00125-014-3468-5 (2015).

42 van der Meulen, T. *et al.* Virgin Beta Cells Persist throughout Life at a Neogenic Niche within Pancreatic Islets. *Cell metabolism* **25**, 911-926 e916, doi:10.1016/j.cmet.2017.03.017 (2017).

43 Blum, B. *et al.* Reversal of beta cell de-differentiation by a small molecule inhibitor of the TGFbeta pathway. *eLife* **3**, e02809, doi:10.7554/eLife.02809 (2014).

44 Tran Thi Nhu, H., Arrojo, E. D. R., Berggren, P. O. & Boudier, T. A novel toolbox to investigate tissue spatial organization applied to the study of the islets of Langerhans. *Scientific reports* **7**, 44261, doi:10.1038/srep44261 (2017).

45 Westacott, M. J. *et al.* Age-Dependent Decline in the Coordinated [Ca(2+)] and Insulin Secretory Dynamics in Human Pancreatic Islets. *Diabetes* **66**, 2436-2445, doi:10.2337/db17-0137 (2017).

Figure 1

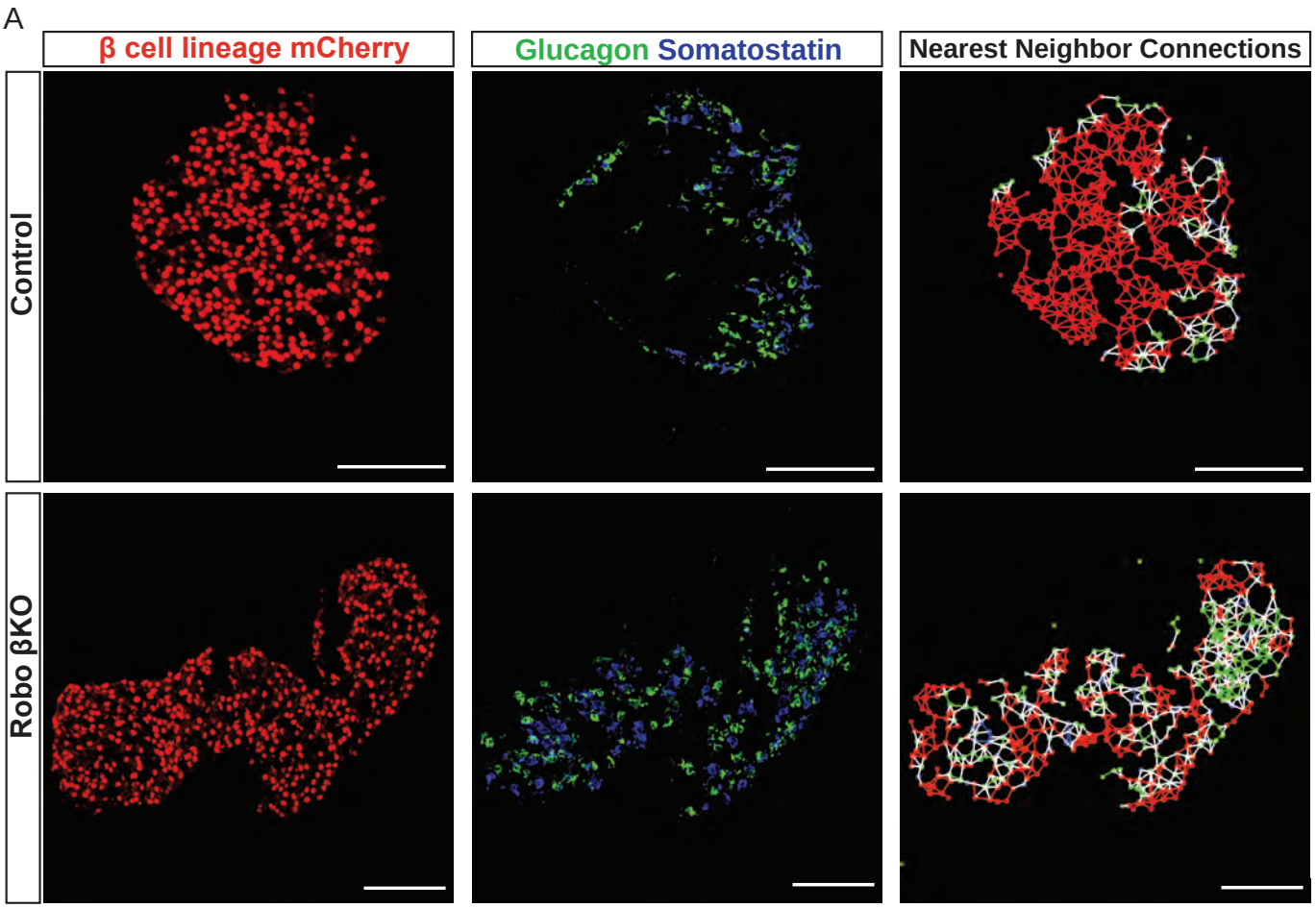

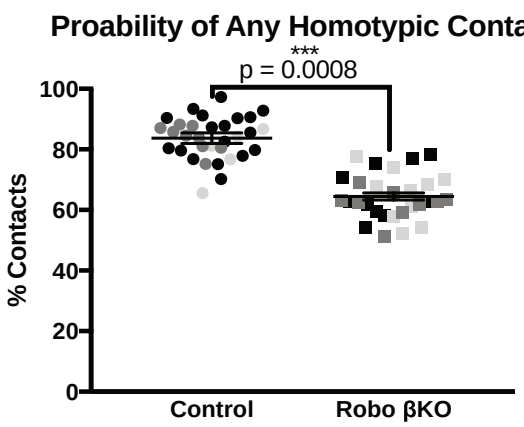

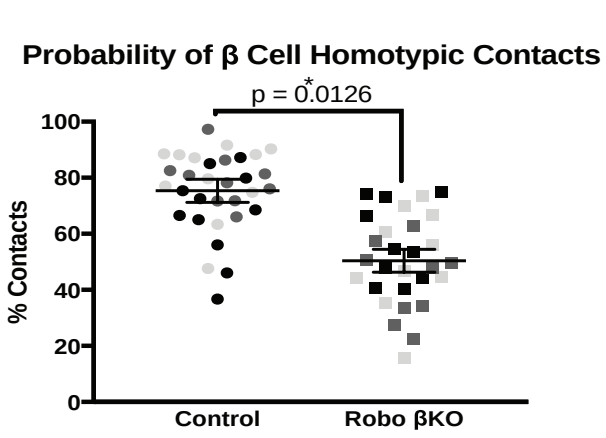

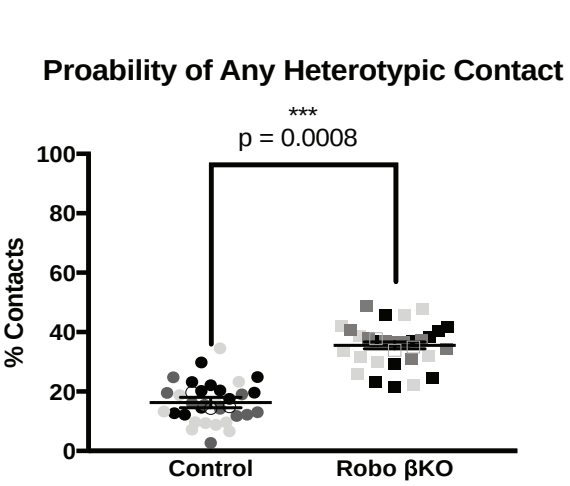

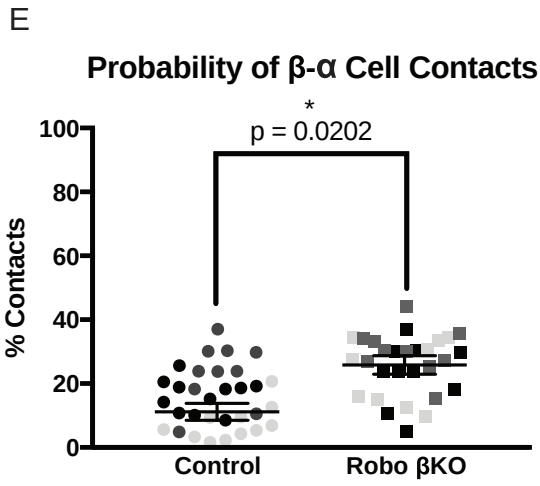

Figure 2

A

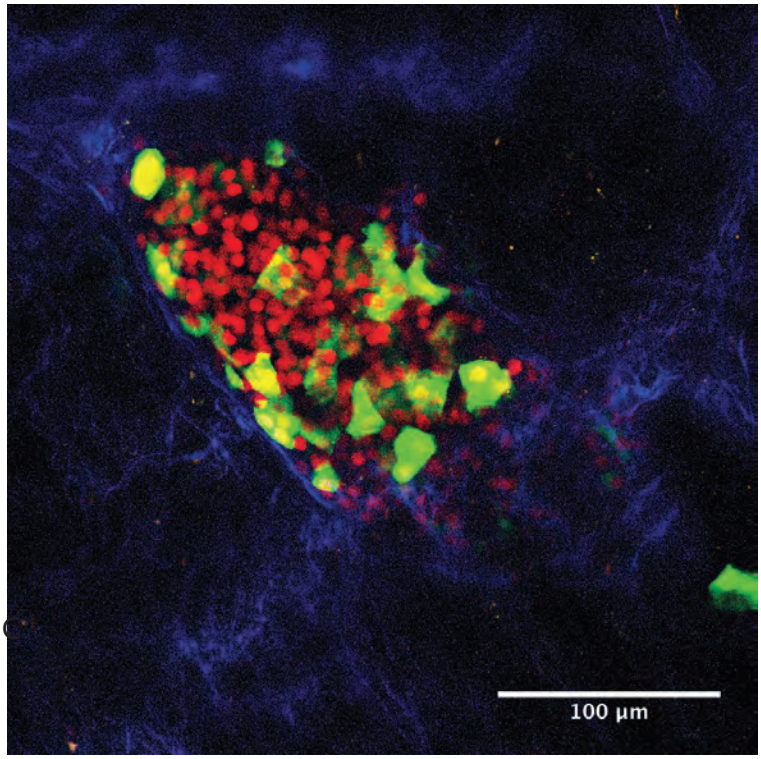

B

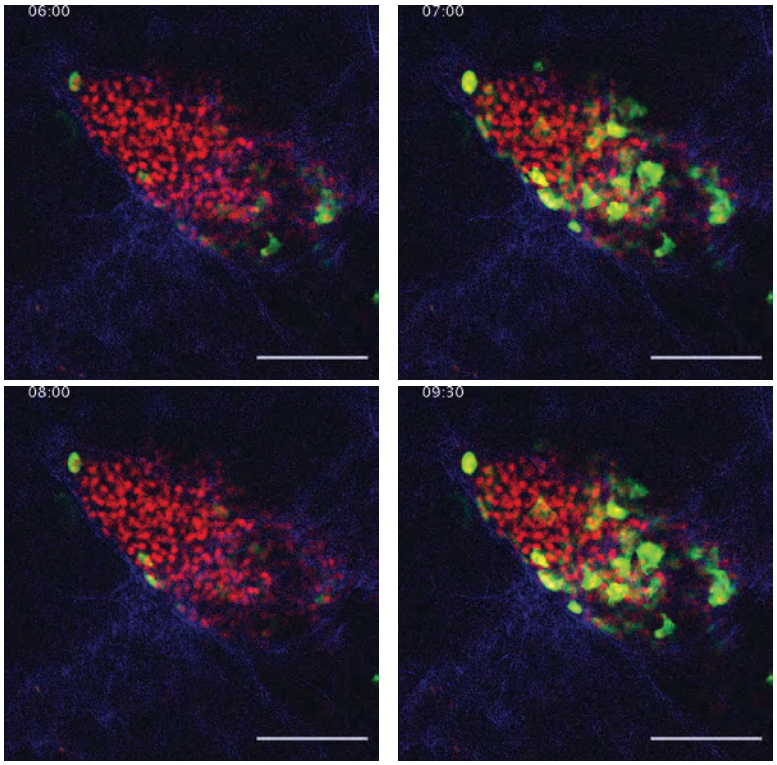

C

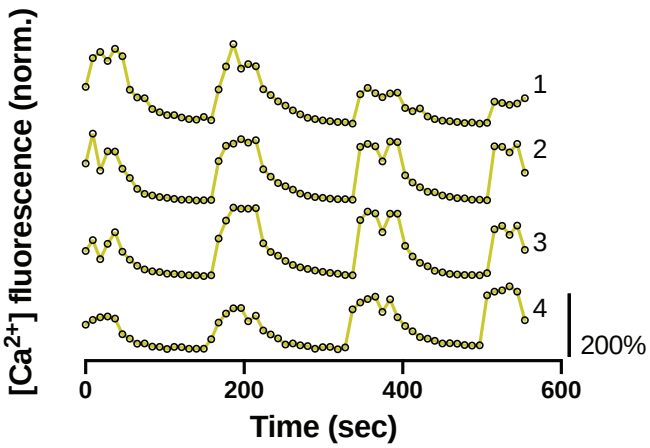

D

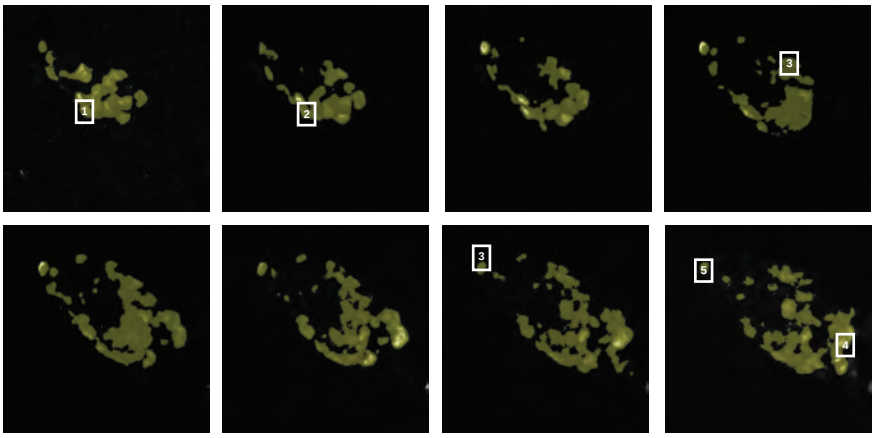

Figure 3

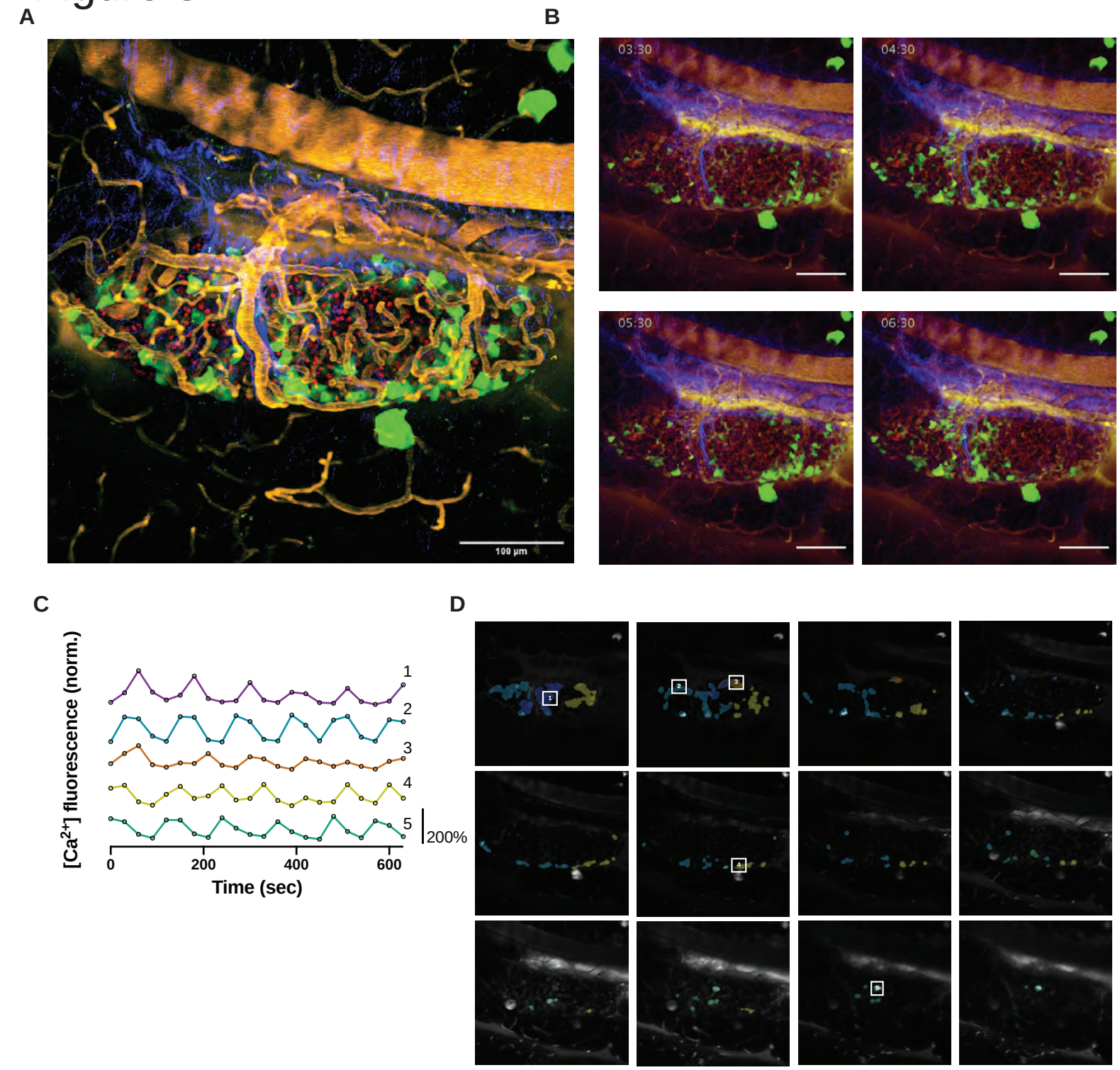

Figure 4

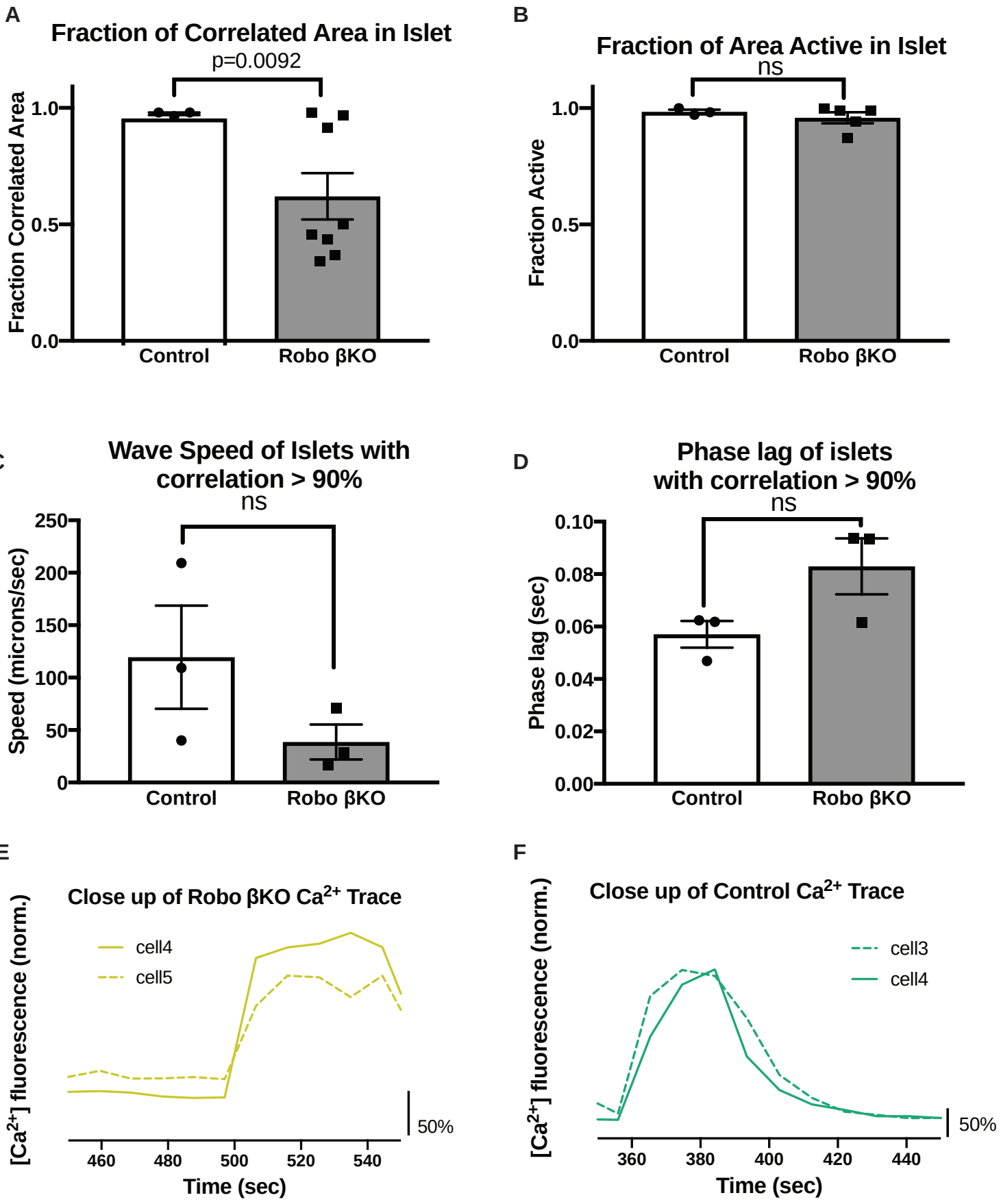

Figure 5

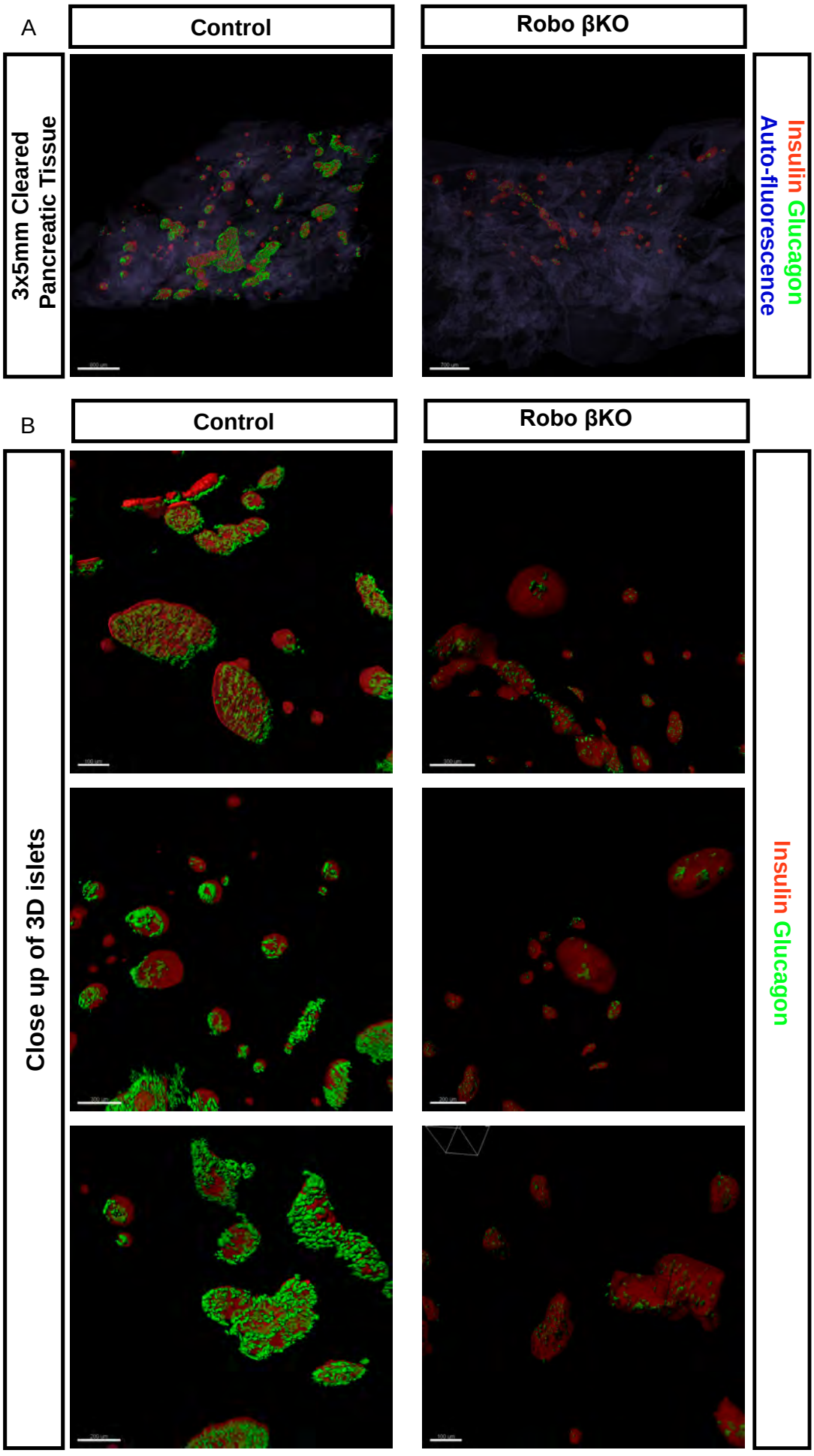

Figure 6

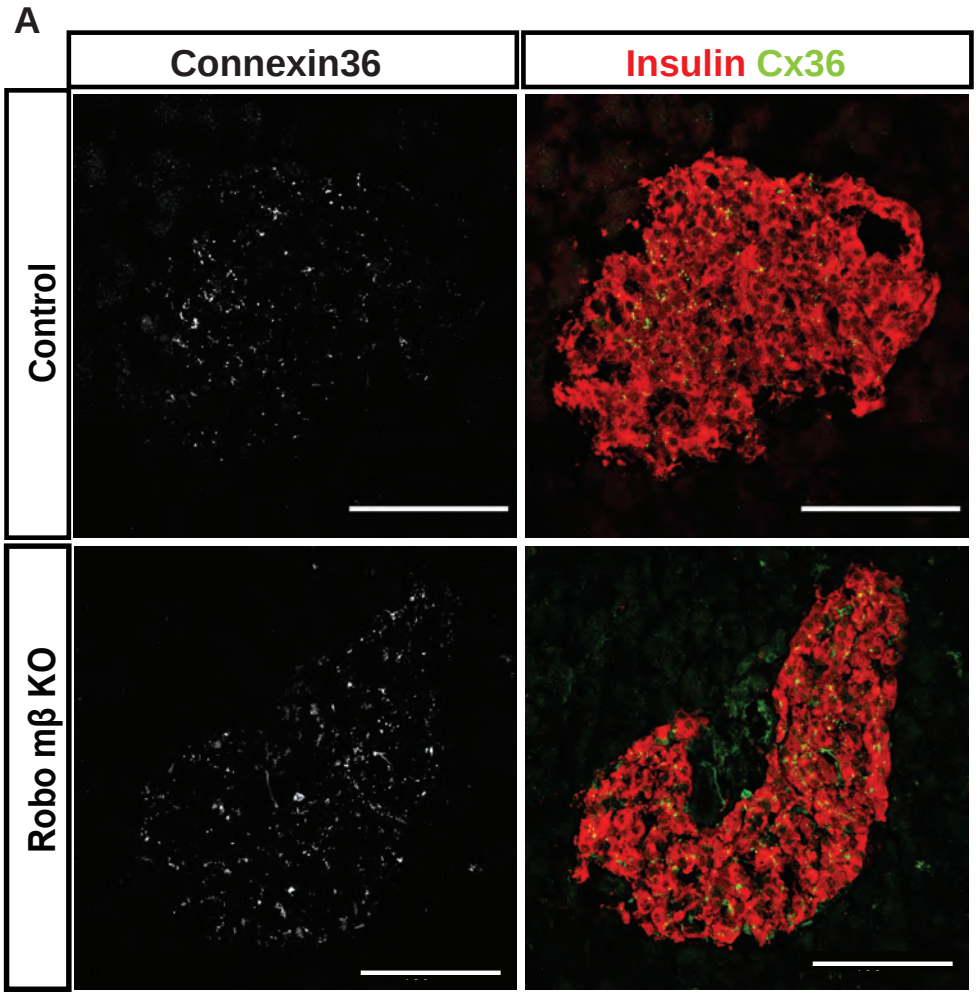

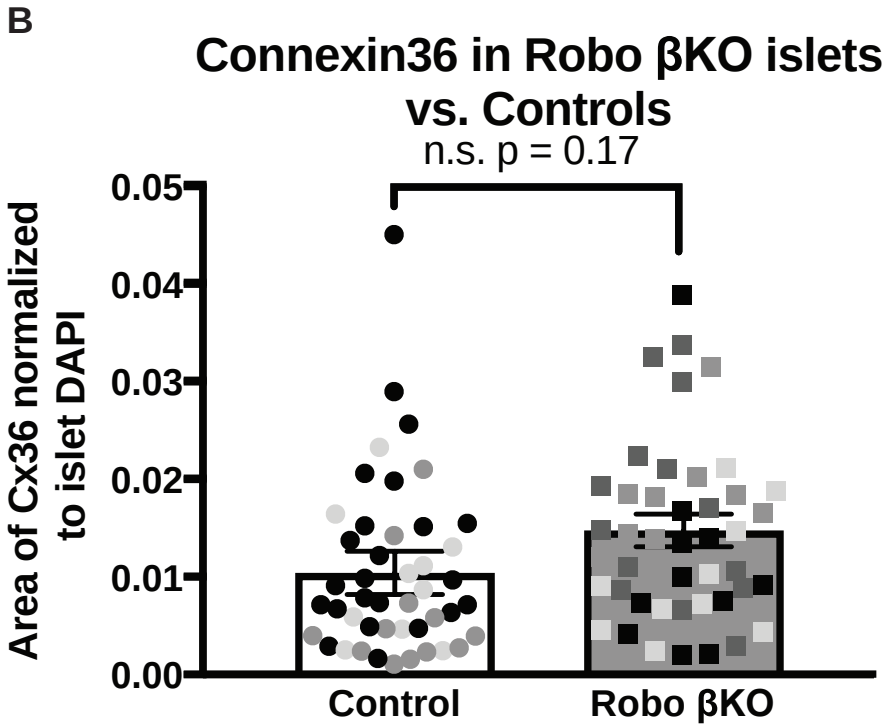

Figure 7